

Distinct representations of olfactory information in different cortical centres

Dara L. Sosulski¹, Maria Lissitsyna Bloom^{1,†}, Tyler Cutforth^{1,†}, Richard Axel¹ & Sandeep Robert Datta^{1,†}

Sensory information is transmitted to the brain where it must be processed to translate stimulus features into appropriate behavioural output. In the olfactory system, distributed neural activity in the nose is converted into a segregated map in the olfactory bulb^{1–3}. Here we investigate how this ordered representation is transformed in higher olfactory centres in mice. We have developed a tracing strategy to define the neural circuits that convey information from individual glomeruli in the olfactory bulb to the piriform cortex and the cortical amygdala. The spatial order in the bulb is discarded in the piriform cortex; axons from individual glomeruli project diffusely to the piriform without apparent spatial preference. In the cortical amygdala, we observe broad patches of projections that are spatially stereotyped for individual glomeruli. These projections to the amygdala are overlapping and afford the opportunity for spatially localized integration of information from multiple glomeruli. The identification of a distributive pattern of projections to the piriform and stereotyped projections to the amygdala provides an anatomical context for the generation of learned and innate behaviours.

In vision and touch, information central to perception is ordered in space in the external world and this order is maintained from the peripheral sense organs to the cortex. Olfactory information, however, does not exhibit a discernible spatial order in the physical world and this poses the question of how odours are represented in the brain. In mammals, olfactory perception is initiated by the recognition of odorant molecules by a large repertoire of receptors in the olfactory sensory epithelium⁴. Individual olfactory sensory neurons express one of approximately 1,000 receptors^{5–7}, and each receptor interacts with multiple odorants. Neurons expressing a given receptor, although randomly distributed within zones of the olfactory epithelium, project with precision to two spatially invariant glomeruli in the olfactory bulb^{1–3}. Thus, the randomly distributed population of neurons activated by an odorant in the olfactory epithelium is consolidated into a discrete stereotyped map of glomerular activity in the olfactory bulb^{8,9}.

This highly ordered map of spatially invariant glomeruli must then be transformed in higher olfactory centres. The projection neurons of the olfactory bulb, mitral and tufted cells, extend an apical dendrite into a single glomerulus and send axons to several telencephalic areas, including a significant input to the piriform cortex and cortical amygdala^{10–15}. Electrophysiological studies and optical imaging reveal that individual odorants activate subpopulations of neurons distributed across the piriform without spatial preference^{16,17}. The piriform therefore discards the spatial segregation of the bulb and returns to a highly dispersed organization in which different odorants activate unique ensembles of cortical neurons. However, the patterns of neural activity do not allow us to discern whether mitral and tufted cell projections from a given glomerulus to cortical neurons are segregated or distributed, and whether they are random or determined. Distinguishing between these possibilities is important for understanding odour perception because a random representation of odour identity could accommodate learned olfactory

behaviours, but is unlikely to specify innate behaviours. Rather, innate olfactory behaviours are likely to result from the activation of genetically determined, stereotyped neural circuits. We have therefore developed a strategy to trace the projections from identified glomeruli in the olfactory bulb to higher olfactory cortical centres.

Mitral and tufted cells that innervate a single glomerulus were labelled by electroporation of tetramethylrhodamine (TMR)-dextran under the guidance of a two-photon microscope. This technique labels mitral and tufted cells that innervate a single glomerulus and is sufficiently robust to allow the identification of axon termini within multiple higher order olfactory centres (Figs 1a–c, 2 and Supplementary Figs 1–4). Labelling of glomeruli in the olfactory bulbs of mice that express GFP under the control of specific odorant receptor promoters permits us to examine potential stereotypy of projections from identical glomeruli (MOR28–IRES–GFP ($n = 8$), MOR1–3–IRES–GFP ($n = 13$), and MOR174–9–IRES–GFP ($n = 10$))¹⁸. Labelling of random unidentified glomeruli was performed in mice expressing synapto-pHluorin (OMP–IRES–spH), a fluorescent marker that allows us to visualize individual glomeruli⁹. This permits us to sample the projection patterns from multiple different glomeruli (Fig. 1c).

Electroporation of a single glomerulus results in the labelling of 6–17 neurons in the mitral cell layer (mean = 9.2 ± 0.8 ; Fig. 1e and

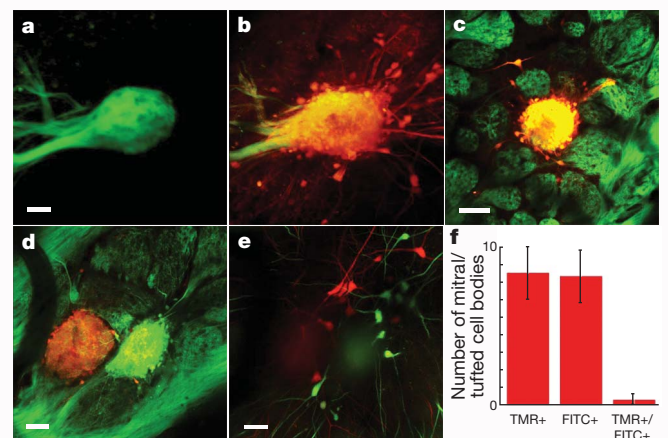


Figure 1 | Targeted electroporation of TMR-dextran labels cells that innervate a single glomerulus in the olfactory bulb. **a, b,** A mouse olfactory bulb in which the MOR174–9 glomerulus is labelled with GFP, before **(a)** and after **(b)** electroporation with TMR-dextran. Scale bar, 40 μm . **c,** Image similar to **a** where electroporation was performed in a mouse in which spH is expressed in all glomeruli (OMP–IRES–spH, green); note that labelling (red) is confined to a single glomerulus. Scale bar, 85 μm . **d,** Control experiment in an OMP–IRES–spH mouse in which neighbouring glomeruli were electroporated with TMR-dextran (red, left) and FITC-dextran (green, right). Scale bar, 45 μm . **e,** Labelling of mitral cells (red, green) as a result of the experiment in **d**. **f,** Quantification of the overlap in mitral cell labelling in experiments similar to **d** (error bars represent s.e.m.; $n = 4$).

¹Department of Neuroscience and the Howard Hughes Medical Institute, College of Physicians and Surgeons, Columbia University, New York, New York 10032, USA. †Present addresses: Department of Neurobiology, Harvard Medical School, Boston, Massachusetts 02115, USA (M.L.B., S.R.D.); Department of Molecular, Cell and Developmental Biology, University of California, Santa Cruz, California 95064, USA (T.C.).

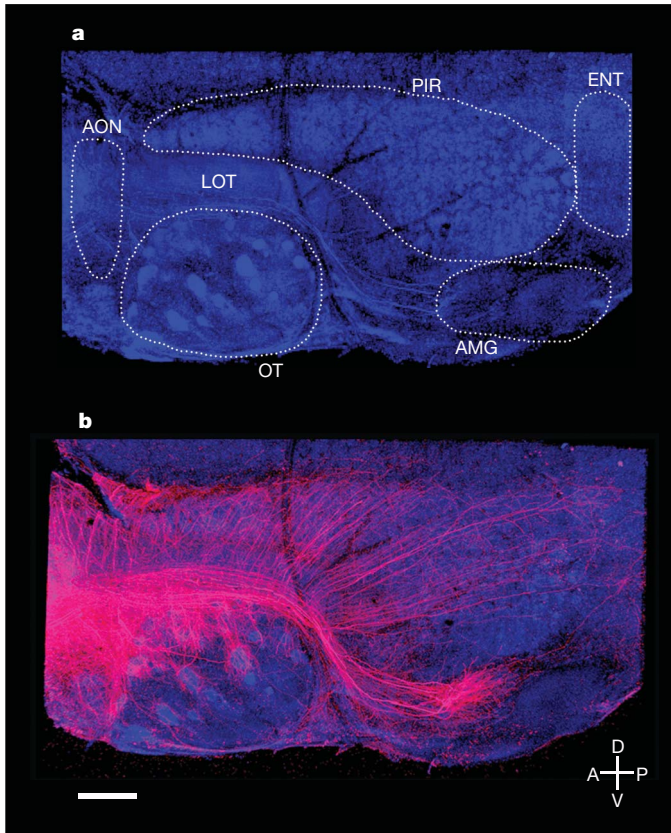


Figure 2 | Mitral/tufted cells connected to a single glomerulus show distinct patterns of projections to several areas of the olfactory cortex. **a**, A flattened hemi-brain preparation of the olfactory cortex with nuclei identified by counterstain (blue, NeuroTrace 435) and relevant structures outlined in white. AON, anterior olfactory nucleus; AMG, cortical amygdala; ENT, lateral entorhinal cortex; LOT, lateral olfactory tract; OT, olfactory tubercle; PIR, piriform cortex. **b**, A hemi-brain from a mouse in which a single glomerulus was electroporated with TMR-dextran (red). Note the unique pattern of projection in each of the olfactory areas. A, anterior; P, posterior; D, dorsal; V, ventral. Scale bar, 700 μm . See also Supplementary Fig. 3.

Supplementary Figs 1c, 2; see Methods). We have demonstrated that all mitral and tufted cells labelled in this manner innervate a single glomerulus by electroporating TMR-dextran into one glomerulus and fluorescein isothiocyanate (FITC)-conjugated dextran into a neighbouring glomerulus (Fig. 1d). Examination of the mitral and tufted cells after this two-colour electroporation reveals either red or green mitral and tufted cells with only a rare cell labelled simultaneously with the two dyes (1/60 cells, $n = 4$) (Fig. 1e, f). This labelling strategy therefore restricts incorporation of tracer to mitral and tufted cells innervating only one glomerulus.

We observe that projections from individual glomeruli extend to all major olfactory cortical regions including the accessory olfactory nucleus, piriform cortex, olfactory tubercle, cortical amygdala and lateral entorhinal cortex (Fig. 2b and Supplementary Fig. 3). Visualization of the extent of axonal projections was facilitated by the development of a flattened hemi-brain preparation that enables high-resolution imaging of all olfactory centres except the anterior olfactory nucleus, which is obscured by the overlying lateral olfactory tract (LOT). The glomeruli we examined project to all the major olfactory cortical regions independent of the spatial location of the glomerulus within the olfactory bulb ($n = 21$ different glomeruli in the flattened preparation; see later). Each of the different higher olfactory centres receives a qualitatively unique pattern of input from the olfactory bulb (Fig. 2b and Supplementary Fig. 3). In the piriform cortex a distributive representation is observed, whereas in the amygdala mitral cell projections are broad but spatially segregated.

Mitral and tufted cell axons extend to the piriform cortex via the LOT. We observe that axonal branches exit the LOT at right angles and extend upward to densely and diffusely project to the piriform cortex along the entire anteroposterior axis (Fig. 3a–c), with no apparent spatial preference in any dimension. High-resolution multiphoton imaging reveals varicosities likely to be axonal boutons (Supplementary Fig. 4). The spatial distribution of these varicosities is similar in every field imaged and is independent of glomerular origin, indicating that mitral and tufted cell synapses with piriform neurons are distributed throughout the piriform cortex (Supplementary Fig. 5). The density of these varicosities within the piriform cortex is also similar regardless of the identity of the electroporated glomerulus, further suggesting that each glomerulus makes a similar number of synapses (MOR1-3, $10.2 \pm 0.57 \mu\text{m}$ of axon per varicosity; M72 mouse 1, 9.9 ± 0.65 ; and M72 mouse 2, $10.1 \pm 0.36 \mu\text{m}$ of axon per varicosity; Supplementary Figs 4, 5). The highly dispersed pattern of projection to the piriform cortex is observed from every glomerulus examined independent of its identity or location within the olfactory bulb ($n = 21$; Supplementary Fig. 6). On visual inspection, the patterns of projection from two identical glomeruli are no more similar than the patterns of projection observed from two different glomeruli.

We performed hierarchical and k -means clustering to determine whether the observed patterns of projections from different glomeruli are quantitatively distinguishable (see Methods). We were unable to identify any parameters, including axon fibre positions, density of TMR labelling, centre of mass X and Y coordinates and centroid X and Y coordinates, that reliably distinguish the projection patterns from different glomeruli (Supplementary Table 1). All measured parameters were similar on comparison of the projection patterns from identical or different glomeruli (Supplementary Fig. 7).

Cross-correlation analysis was performed to compare the patterns of piriform projections from different glomeruli (see Methods and Supplementary Fig. 8 for detailed explanation of method and interpretation). The correlograms comparing identical and distinct glomeruli show an extended region of moderate correlation (Fig. 3d–f). These data indicate that the dispersed pattern of projections is largely homogeneous in density over several spatial scales (Supplementary Fig. 9) and indicate that the patterns are similar for each of the 24 glomeruli we examined. The similarity of correlograms from identical and different glomeruli provides further evidence that the pattern of piriform projections does not differ for each of the distinct glomerulus types. Thus, the mitral cells innervating an individual glomerulus discard the insular and invariant spatial segregation of the bulb and project dense, dispersed axons to the piriform cortex with no discernible spatial bias.

Next we examined the patterns of projections of single glomeruli to the cortical amygdala. The cortical amygdala consists of three nuclei: the anterior cortical, posterolateral cortical and posteromedial cortical nuclei. The posteromedial cortical nucleus, a major site of innervation from the accessory olfactory bulb¹⁹, receives no discernible input from any of the glomeruli of the main olfactory bulb we examined (Fig. 4a–c, d–f, $n = 33$ glomeruli in the en face preparation, see Methods), and we observe relatively sparse projections anterior to the posterolateral nucleus. We therefore restrict our analysis to the posterolateral cortical nucleus. The patterns of projection from individual glomeruli in the posterolateral nucleus reveal dense, patchy axonal projections that have a focal nexus surrounded by a less dense halo of fibres (Fig. 4a–f). Despite the diffuse nature of projections, different glomeruli appear to send fibres to anatomically distinct and spatially invariant regions of the posterolateral cortical amygdala (Fig. 4a–f). For example, projections from the MOR1-3 glomerulus consistently occupy the most medial aspect of the posterolateral nucleus, whereas projections from the MOR28 glomerulus terminate more laterally. These conclusions are evident on visual inspection and are supported by more quantitative analysis.

k -means clustering using relevant parameters extracted from the amygdala projection patterns after image alignment (centre of mass

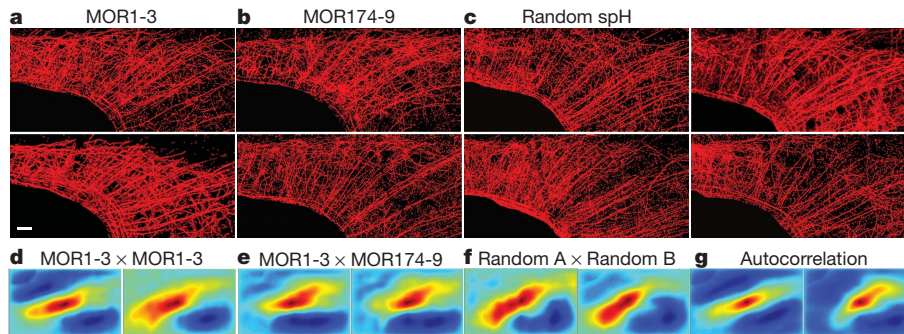


Figure 3 | Projections from single glomeruli to piriform cortex are disperse, homogeneous and indistinguishable. **a–c**, Images of axons innervating the piriform cortex (red) from mitral and tufted cells that connect to the glomerulus corresponding to MOR1-3 (**a**), MOR174-9 (**b**) or a random selection of glomeruli labelled with TMR-dextran (**c**). Scale bar, 500 μm . **d–f**, Correlograms plotted using the matrix of correlation coefficients generated

by normalized cross-correlation of two MOR1-3 piriforms (**d**), a MOR1-3 and a MOR174-9 piriform (**e**), and two piriforms in which random glomeruli were labelled (**f**). Cross-correlation is performed using aligned images of projection patterns as seen in **a–c**. **g**, Autocorrelograms generated using methods from **d** in which a labelled piriform is compared to itself. Note that correlograms in **g** are essentially indistinguishable from the correlograms in **d–f**.

X coordinate, X position of medial-most fibre, absolute medial fibre density, ratio of lateral/medial fibre density) was performed on the projections from three identified glomeruli, MOR1-3 ($n = 5$), MOR174-9 ($n = 5$) and MOR28 ($n = 4$). This cluster analysis correctly assigns glomerular identity for 79% of the samples examined (one-way MANOVA, $P = 0.0006$, $\alpha = 0.05$).

We performed normalized cross-correlation analysis to compare further the projection patterns from different glomeruli. Cross-correlation analysis reveals a single peak in the correlogram that reflects the more focal nature of projections to this brain region than in the piriform (Fig. 4g–j). The correlograms between the projection patterns of identical glomeruli reveal peaks that show a small displacement from the centre (Fig. 4g, h, Supplementary Figs 10, 11a–c, 12g, h and Supplementary Tables 2, 3). Cross-correlation using images of projection patterns from different glomeruli show more varied and often very large displacements (Fig. 4i, Supplementary Figs 10, 11d–j, 12i and Supplementary Tables 2, 3). These data indicate that the cortical amygdala receives spatially stereotyped projections from individual glomeruli. Although individual glomeruli project to fixed positions, extensive overlap is observed for the projections from different glomeruli. The apparently random pattern of projections in the piriform and the determined pattern in the amygdala are likely to

provide the anatomical substrates for distinct olfactory-driven behaviours mediated by these two brain regions.

Insight into the logic of olfactory perception will depend on an understanding of how the highly ordered glomerular map is represented in higher olfactory centres. Previous experiments have used the injection of tracer molecules into the bulb or cortex to relate the spatial position of projection neurons in the bulb with their targets in higher olfactory centres^{10–15}. These experiments predate the ability to identify specific glomeruli², precluding a determination as to whether projections from a single mitral/tufted cell or a single glomerulus are random or stereotyped.

We have defined a neural circuit that conveys olfactory information from specific glomeruli in the olfactory bulb to the piriform cortex and the cortical amygdala. A distributive representation of neurons in the sensory epithelium is converted into a topographical map in the bulb on the convergence of like axons onto spatially invariant glomeruli^{1,2}. The piriform discards this spatial order; axons from individual glomeruli project diffusely to the piriform without apparent spatial preference. Neurons from every glomerulus elaborate similar axonal arborizations and quantitative analyses fail to identify features that may distinguish the individual projection patterns. These data are in accordance with retrograde tracings using rabies virus that reveal the convergence of multiple, spatially distributed glomeruli on a small number of piriform

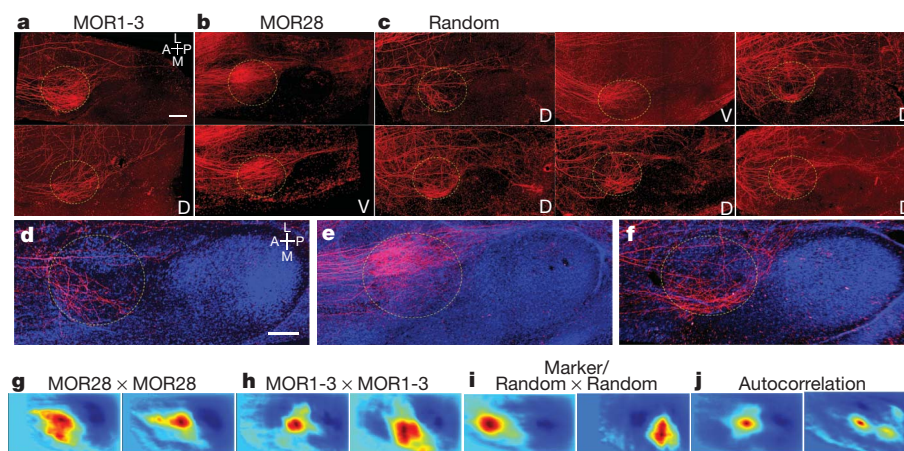


Figure 4 | Projections from single glomeruli to the cortical amygdala are broad, patchy and stereotyped. **a–c**, Images of the cortical amygdala reveal similar projections from the mitral and tufted cells that connect to the MOR1-3 glomerulus in two different brains (circle represents the approximate posterolateral cortical nucleus boundary) (**a**), but projections that are distinct from those of mitral/tufted cells connected to the MOR28 glomerulus (**b**) or six randomly selected glomeruli (**c**). ‘D’ or ‘V’ in the bottom right corner of the image indicates whether the electroporated glomerulus was located dorsally or ventrally in the bulb. M, medial; L, lateral. Scale bar, 400 μm . **d–f**, Counterstained images

from a subregion of images in **a–c** showing a closer view of projection patterns. Scale bar, 400 μm . **g–i**, Correlograms plotted using the matrix of correlation coefficients generated by normalized cross-correlation of MOR28 \times MOR28 projection patterns within the posterolateral cortical amygdala (PLCo) (**g**), MOR1-3 \times MOR1-3 projection patterns (**h**), or projection patterns from glomeruli of different types (**i**). **j**, Autocorrelograms of the PLCo from two labelled glomeruli correlated with themselves. Note that in the en bloc preparation shown here, the lateral/medial axis (indicated by the orientation bars) is synonymous with the dorsal/ventral axis, as this region of brain is curved.

neurons²⁰. A distributive representation of glomerular projections in the piriform is also observed on anterograde tracing of individual mitral cells after Sindbis virus infection²¹.

Optical imaging and electrophysiological studies of neural responses to odours reflect these anatomical transformations. Distributed neural activity in the sensory epithelium of the nose is transformed in the bulb, with each odour eliciting distinct spatial patterns of glomerular activity^{8,9}. A second transformation is apparent in the piriform cortex where individual odourants activate unique ensembles of neurons that are distributed without discernible spatial order^{16,17}. These neurons also exhibit discontinuous receptive fields; neurons within an ensemble responsive to a given odour respond to multiple, structurally dissimilar odours^{16,22}. The dispersed projections to the piriform provide an anatomical substrate for the generation of these patterns of neural activity.

One model consistent with both the anatomy and physiology invokes the random convergence of excitatory inputs from mitral cells onto piriform neurons such that each piriform neuron would sample a random combination of glomerular inputs. If the connections from bulb to cortex are indeed random, then the representation of the quality of an odourant or its valence in the piriform must be imposed by experience. Odourants, however, can elicit innate behavioural responses, indicating that a second area of the brain must receive determined inputs from the olfactory bulb. The pattern of projections to the posterolateral amygdala implicates this structure in the generation of innate olfactory-driven behaviours. This suggestion is in accordance with the finding that disruption of the amygdala abrogates innate, odour-driven behaviours but leaves learned olfactory responses intact^{23,24}.

The olfactory circuits we describe in the mouse are reminiscent of the architecture of the olfactory system in *Drosophila*²⁵, despite the six hundred million years of evolution that separate the two organisms. In *Drosophila*, neurons expressing a given odourant receptor are distributed throughout the antenna and converge on spatially invariant glomeruli in the antennal lobe. Information from the antennal lobe bifurcates, with one branch exhibiting spatially invariant projections to the lateral horn, a brain region mediating innate olfactory behaviours. A second branch projects to the mushroom body, a structure required for learned olfactory responses. This anatomical and functional bifurcation provides a context in which to consider the generation of the various forms of olfactory-driven behaviour in both flies and mice. Our data indicate that innate olfactory behaviours derive from determined neural circuits selected over evolutionary time, whereas learned behaviours may be mediated by the selection and reinforcement of random ensembles of neurons over the life of an organism.

METHODS SUMMARY

Single glomeruli and their associated mitral and tufted cells were labelled in adult mice via electroporation of 3 kD TMR-dextran (Invitrogen) under a two-photon microscope (Prairie Technologies). Glass electrodes were backfilled with dye and guided to a glomerulus centre, and current was applied to the back of the pipette (50 V, 30-ms pulses, 2Hz, 7–10 min, repeated 2–4 times, Grass Technologies). Afterwards, mice were allowed to recover for 5 days before being killed. Excised brains were prepared for imaging either by flattening the cortex of the right hemisphere or surgical excision of the cortical amygdala. TMR-dextran signal was amplified by antibody staining (Jackson Immunoresearch), and samples were counterstained (NeuroTrace 435, Invitrogen). Images were acquired using multiphoton excitation on a Zeiss 710 or a Prairie *in vivo* microscope. Image z-stacks of the piriform cortex or cortical amygdala were aligned using SPM8 and Photoshop, and then quantified using ImageJ and custom-written Matlab code (Mathworks).

Full Methods and any associated references are available in the online version of the paper at www.nature.com/nature.

Received 2 November 2010; accepted 25 January 2011.

Published online 30 March 2011.

1. Ressler, K. J., Sullivan, S. L. & Buck, L. B. Information coding in the olfactory system: evidence for a stereotyped and highly organized epitope map in the olfactory bulb. *Cell* **79**, 1245–1255 (1994).

2. Mombaerts, P. *et al.* Visualizing an olfactory sensory map. *Cell* **87**, 675–686 (1996).
3. Vassar, R. *et al.* Topographic organization of sensory projections to the olfactory bulb. *Cell* **79**, 981–991 (1994).
4. Buck, L. & Axel, R. A novel multigene family may encode odourant receptors: a molecular basis for odor recognition. *Cell* **65**, 175–187 (1991).
5. Malmic, B., Hirono, J., Sato, T. & Buck, L. B. Combinatorial receptor codes for odors. *Cell* **96**, 713–723 (1999).
6. Chess, A., Simon, I., Cedar, H. & Axel, R. Allelic inactivation regulates olfactory receptor gene expression. *Cell* **78**, 823–834 (1994).
7. Niimura, Y. & Nei, M. Evolutionary changes of the number of olfactory receptor genes in the human and mouse lineages. *Gene* **346**, 23–28 (2005).
8. Rubin, B. D. & Katz, L. C. Optical imaging of odourant representations in the mammalian olfactory bulb. *Neuron* **23**, 499–511 (1999).
9. Bozza, T., McGann, J. P., Mombaerts, P. & Wachowiak, M. *In vivo* imaging of neuronal activity by targeted expression of a genetically encoded probe in the mouse. *Neuron* **42**, 9–21 (2004).
10. Haberly, L. B. & Price, J. L. The axonal projection patterns of the mitral and tufted cells of the olfactory bulb in the rat. *Brain Res.* **129**, 152–157 (1977).
11. Scott, J. W., McBride, R. L. & Schneider, S. P. The organization of projections from the olfactory bulb to the piriform cortex and olfactory tubercle in the rat. *J. Comp. Neurol.* **194**, 519–534 (1980).
12. Price, J. L. An autoradiographic study of complementary laminar patterns of termination of afferent fibers to the olfactory cortex. *J. Comp. Neurol.* **150**, 87–108 (1973).
13. Luskin, M. B. & Price, J. L. The distribution of axon collaterals from the olfactory bulb and the nucleus of the horizontal limb of the diagonal band to the olfactory cortex, demonstrated by double retrograde labeling techniques. *J. Comp. Neurol.* **209**, 249–263 (1982).
14. Buonviso, N., Reval, M. F. & Jourdan, F. The projections of mitral cells from small local regions of the olfactory bulb: an anterograde tracing study using PHA-L (*Phaseolus vulgaris* Leucoagglutinin). *Eur. J. Neurosci.* **3**, 493–500 (1991).
15. Ojima, H., Mori, K. & Kishi, K. The trajectory of mitral cell axons in the rabbit olfactory cortex revealed by intracellular HRP injection. *J. Comp. Neurol.* **230**, 77–87 (1984).
16. Stettler, D. D. & Axel, R. Representations of odor in the piriform cortex. *Neuron* **63**, 854–864 (2009).
17. Rennaker, R. L., Chen, C. F., Ruyle, A. M., Sloan, A. M. & Wilson, D. A. Spatial and temporal distribution of odourant-evoked activity in the piriform cortex. *J. Neurosci.* **27**, 1534–1542 (2007).
18. Shykind, B. M. *et al.* Gene switching and the stability of odourant receptor gene choice. *Cell* **117**, 801–815 (2004).
19. de Olmos, J., Hardy, H. & Heimer, L. The afferent connections of the main and the accessory olfactory bulb formations in the rat: an experimental HRP-study. *J. Comp. Neurol.* **181**, 213–244 (1978).
20. Miyamichi, K. *et al.* Cortical representations of olfactory input by trans-synaptic tracings. *Nature* advance online publication, doi:10.1038/nature09714 (22 December 2010).
21. Ghosh, S. *et al.* Sensory maps in the olfactory cortex defined by long-range viral tracing of single neurons. *Nature* advance online publication doi:10.1038/nature09945 (30 March 2011).
22. Poo, C. & Isaacson, J. S. Odor representations in olfactory cortex: “sparse” coding, global inhibition, and oscillations. *Neuron* **62**, 850–861 (2009).
23. Blanchard, D. C. & Blanchard, R. J. Innate and conditioned reactions to threat in rats with amygdaloid lesions. *J. Comp. Physiol. Psychol.* **81**, 281–290 (1972).
24. Slotnick, B. M. Olfactory discrimination in rats with anterior amygdala lesions. *Behav. Neurosci.* **99**, 956–963 (1985).
25. Vossahl, L. B. & Stocker, R. F. Molecular architecture of smell and taste in *Drosophila*. *Annu. Rev. Neurosci.* **30**, 505–533 (2007).

Supplementary Information is linked to the online version of the paper at www.nature.com/nature.

Acknowledgements We thank members of the R.A. and S.R.D. laboratories for comments and advice, B. Shykind for mice with GFP-labelled olfactory receptor neurons, S. X. Luo for image alignment advice, D. M. Bear for cross-correlation analysis advice, D. Padfield for Matlab code, R. Wilson for comments on the manuscript and P. Kisloff for manuscript preparation assistance. Financial support was provided by a Helen Hay Whitney Foundation Fellowship, a Career Award in the Medical Sciences grant from the Burroughs Wellcome Fund, and funding from the National Institutes of Health through the NIH Director’s New Innovator Award Program (DP2-OD-007109) (S.R.D.), a Ruth L. Kirschstein National Research Service Award predoctoral fellowship from the National Institutes of Health (D.L.S.), and the Howard Hughes Medical Institute and a grant from the Foundation for the National Institutes of Health through the Grand Challenges in Global Health initiative (R.A.).

Author Contributions S.R.D., D.L.S. and R.A. conceived the project, participated in its development and wrote the manuscript. S.R.D. and D.L.S. developed methods and performed all experiments and data analysis. T.C. generated the MOR1-3 and MOR174-9-IRES-GFP mice. M.L.B. performed mouse husbandry and immunostaining.

Author Information Reprints and permissions information is available at www.nature.com/reprints. The authors declare no competing financial interests. Readers are welcome to comment on the online version of this article at www.nature.com/nature. Correspondence and requests for materials should be addressed to R.A. (ra27@columbia.edu).

METHODS

Surgery. Mice were anaesthetized with ketamine/xylazine (100 mg kg⁻¹ or 10 mg kg⁻¹, respectively; Sigma-Aldrich), and temperature was maintained at 37 °C on a feedback-controlled heating pad (Fine Science Tools). The scalp was removed, and membrane overlying the skull was cleared using a microblade (Roboz). An aluminium headpost cut from square bar (Small Parts) was attached to the skull using RelyX luting cement (Henry Schein). The borders of the exposure were covered with silicone sealant (VWR). For dorsal glomeruli, the skull overlying the olfactory bulb was thinned using a dental drill (KaVo) and removed with forceps, and the dura was peeled back using fine forceps (Roboz). For lateral glomeruli, the skin overlying the cheek and zygomatic bone was removed, and vessels were cauterized (Fine Science Tools). The muscle attached to the zygomatic was peeled away, and the bone was removed with microscissors (Roboz). The eye and surrounding tissue was removed with microscissors; bleeding was stopped using gelfoam (Henry Schein), and mice were administered 0.7 ml Ringer's solution (Henry Schein). The skull overlying the bulb was thinned and removed, and the dura peeled away. After electroporation, the bulb was coverslipped and covered in 2% agarose (Sigma-Aldrich), the exposure was covered in lidocaine jelly (Henry Schein) and then silicone sealant. Buprenorphine (0.05 mg kg⁻¹, Henry Schein) was administered after the mouse could right itself. Mice recovered for 5 days after electroporation, and were then deeply anaesthetized with ketamine/xylazine and killed by paraformaldehyde perfusion.

Electroporation. Mice were placed under a two-photon microscope (Ultima, Prairie Technologies), and a ×16 objective was used to focus on a single glomerulus (.8NA, Nikon). A Ti-Sapphire laser (Coherent) was tuned to 880 nm for experiments. Pulled glass pipets (Sutter, 5–6 μm tip) were backfilled with either lysine-fixable TMR-dextran (3 kDa, 12.5 mg ml⁻¹ in PBS) with biotin or lysine-fixable FITC-dextran (3,000 MW, 12.5 mg ml⁻¹ in PBS) with biotin (Invitrogen), and filled halfway with 0.9% w/v NaCl. The pipette was mounted on an electrode holder (WPI)/manipulator (Luigs and Neumann), and its tip was directed to the three-dimensional centre of a glomerulus under two-photon guidance. Current was applied to the pipette using a stimulator (50 V, 30-ms pulses, at 2 Hz, repeated 2–4 times, Grass SD-9 stimulator). The black lead of the stimulator was connected to the animal via an alligator clip on the foot. Note that although we observed robust and reliable long-range diffusion/transport of TMR-dextran from labelled mitral and tufted cells to the olfactory cortex under these electroporation conditions, FITC-dextran showed substantively less diffusion/transport (for example, few or no labelled fibres in the LOT), which precluded the use of FITC-dextran to explore axonal projections from the bulb to the cortex. Mice in which the glomeruli were not clearly labelled, the labelling was non-specific (an exceedingly rare occurrence) or in which labelled mitral cells in the mitral cell layer could not be identified during the course of the experiment were excluded from subsequent analysis.

Histological processing. Mice were killed by transcardial perfusion with 13 ml PBS, followed by 10 ml 1% paraformaldehyde. Brains were extracted and processed differentially depending on the region to be imaged. For imaging of the whole olfactory cortex, the left hemisphere was discarded and the subcortical matter of the right hemisphere was removed using forceps. Cortical tissue above the rhinal sulcus was dissected away, and guide cuts were made with a needle blade (Fine Science Tools). The ventral hemisphere (which includes all of the structures in the olfactory cortex) was then flattened between two slides separated by a 600-μm spacer constructed of #1.5 coverslips. The sample was placed in 4% paraformaldehyde overnight, and then stored in PBS until antibody staining. For imaging of the amygdala, the brain was dissected as previously described, and a needle blade was used to cut along the LOT to excise the olfactory tubercle; an additional cut was made above the cortical nuclei of the amygdala to excise the olfactory amygdala. We use this en bloc preparation of the amygdala to avoid distortions that occur at the ventral edge of the flattened hemi-preparation, where the cortical amygdala resides. This distortion is minimal in the centre of the flattened preparation where the piriform cortex is located. The amygdala was fixed in 4% paraformaldehyde overnight, and then stored in PBS until antibody staining. Before application of antibody, samples were soaked in glycine (1.87 g per 500 ml PBS, Sigma-Aldrich) for 2 h, followed by 1 h in PBS, 30 min in sodium borohydride (0.4 g per 400 ml PBS, Sigma-Aldrich) and 1 h in PBS to quench autofluorescence. The following series of antibodies and washes were then used: primary antibody for 3 days (1:500 rabbit anti-TMR, Invitrogen) in block (2% Triton X-100, 1% bovine serum albumin in PBS), wash 1 day (2% Triton X-100/PBS), secondary antibody for 2 days (1:250 goat anti-rabbit in block, Jackson ImmunoResearch), wash 1 day, and tertiary antibody (1:250 TMR-conjugated donkey anti-goat in block, Jackson ImmunoResearch) and counterstain (1:150 NeuroTrace 435 in block, Invitrogen) for 2 days, followed by 1 day of wash. Samples were mounted in Vectashield (Vector Labs) on a slide with the shallow end of a Lab-Tek chambered coverglass as a coverslip (NUNC).

Quantification of cellular labelling. Two different methods were used to quantify the efficiency of our labelling method. First, after electroporation, we acquired z-stacks from the surface of the olfactory bulb through the mitral cell layer of the bulb (see Supplementary Movie 1), and used these z-stacks to count the number of cell bodies labelled in the mitral cell layer of the olfactory bulb post hoc. We were unable to quantify the number of tufted cells labelled for technical reasons: the brightness and number of cells labelled superior to the mitral cell layer, as well as the brightness of the glomerulus, made it difficult to quantify cell bodies (Supplementary Fig. 1), and the diversity in morphology and location of tufted cells made it difficult to identify them based on visual and depth criteria. Second, previous work has indicated that mitral cell axons travel superior to tufted cell axons in a segregated manner in the LOT and, unlike tufted cell axons, project to areas posterior to the anterior piriform cortex and olfactory tubercle^{26–30}. We observed that near the most posterior aspect of the olfactory tubercle, the axons of presumed mitral cells form a distinct bundle that continues to travel past the tubercle towards the posterior piriform cortex and amygdala (Supplementary Fig. 2a). Therefore, we counted axons corresponding to presumed mitral cells in the posterior aspect of the LOT using a confocal microscope (see Supplementary Fig. 2). We did not quantify the number of presumed tufted cells with this method owing to technical constraints: these individual axons were difficult to optically resolve due to the large number of cells labelled, the high intensity of labelling, their smaller diameter, and the more three-dimensional structure of the presumed tufted cell axon band in the LOT.

Image acquisition. Images were acquired on a Zeiss 710 confocal microscope (Zeiss) using a ×10 water immersion objective (Zeiss 0.45NA) or a Prairie *in vivo* microscope using a ×10 water immersion objective (Olympus 0.6NA). In both cases images were acquired in multiphoton mode using a Coherent laser tuned to 810 nm. Zen software with a custom-written macro was used for acquisition and tiling of images online; LSM 510 software was used for tiling in the event that it needed to be performed post-hoc (Zeiss). Images were also tiled using XUVTools³¹ (Albert-Ludwigs-Universität Freiburg). Images in which clearly labelled mitral cell fibres were not apparent in the LOT adjacent to the posterior piriform cortex were excluded from further study; in all such cases samples showed other signs of poor labelling (that is, poorly filled axonal arborizations).

Image alignment. During all image processing the operator was blind to the glomerular identity of the particular image stack. z-stacks of images of en bloc preparations of the cortical amygdala were aligned using an intensity-based, two-step linear–nonlinear protocol. Image alignment was carried out in Statistical Parametric Mapping 8 (SPM8) (available at <http://www.fil.ion.ucl.ac.uk/spm>), an open-source software package widely used in fMRI research. SPM is validated for a variety of registration tasks, including analysis of the axonal projection patterns of olfactory projection neurons in *Drosophila*³². The linear registration algorithm used a standard 12-parameter algorithm with Gauss-Newton optimization. The nonlinear registration modelled the spatial transformation with a set of basis functions, the discrete sine transformation (DST) and the discrete cosine transformation (DCT), of various spatial frequencies. Typically only a small number of nonlinear iterations were carried out (often less than 100) and the nonlinear regularization value was held relatively high (typically at 100, never below 1), which maximized the relative contribution of the linear alignment to the template. We generated a standardized template brain stack of the cortical amygdala by morphing four individual stacks onto a single high-quality image stack and then averaging the intensity of the resultant five individual stacks. This standardized reference stack was then used to warp all cortical amygdala stacks used in this study. Warping parameters were optimized for each image stack and the quality of warping was assessed by the overlap between the warped brain and the template image in the counterstained image channel only. The major landmarks in this preparation are the posterolateral cortical amygdala, the posteromedial cortical amygdala and the ventral edge of the posterior piriform cortex, all of which were used to judge alignment quality. Images that failed to align based on the counterstain were excluded from the data set. After warp parameters were defined based upon the counterstained channel, the channel containing the TMR-dextran staining was warped using identical parameters. Because after warping most of the data was contained in superficial planes, all analysis was performed on a maximum intensity projection of the warped volume. Alignment of maximal intensity projections of image stacks of the piriform cortex (which were highly anisotropic—that is, 20,000 × 10,000 × 40—precluding accurate volumetric alignment by SPM8) was performed in Photoshop using affine commands (such as zoom and rotate) as well as the “Warp” command, using only the counterstain as a guide to position.

Statistics. All error bars are ± standard error of the mean (s.e.m.). One-way MANOVA was used to test whether multivariate means of variables for different glomerulus types are different at the 0.05 significance level.

Image processing and cluster analysis. During all image processing the operator was blind to the glomerular identity of the particular image stack. Images were

processed by using a semi-supervised algorithm to filament trace the raw warped image stacks using the Imaris software package (Bitplane), slightly dilating the filaments, and then using those slightly dilated filaments to mask the original raw data. Before extraction of parameters, piriform and posterolateral nucleus projection patterns were aligned using the image alignment procedure previously described. Samples that were unable to be aligned due to poor counterstain or extreme physical distortion were excluded from *k*-means analysis. The data were then maximally contrasted so that differences in label intensity were normalized. A number of parameters characterizing the features of the axonal projection patterns to the piriform cortex (*X* and *Y* centre of mass coordinates, *X* and *Y* centroid coordinates, *X* coordinate of most anterior fibre, *Y* coordinate of most posterior fibre at LOT, number of TMR-positive pixels) and amygdala (*X* and *Y* centre of mass coordinates, *X* and *Y* centroid coordinates, *X* coordinate of medial-most fibre, absolute fibre density within the lateral and medial hemispheres of PLCo, ratio of lateral/medial fibre density to total fibre density within the PLCo) were extracted from the aligned and processed images of samples using ImageJ (NIH) and Matlab (Mathworks). No combination of parameters led to correct classification by glomerular type for piriform images, but the following parameters could be used in various combinations with nearly equal measures of success to classify amygdala samples: *X* coordinate of centre of mass, *X* coordinate of medial-most fibre, absolute fibre density within the medial hemisphere of PLCo, and the ratios of fibre density within the medial or lateral hemispheres to the total fibre density within the PLCo. The standardized Euclidean distance between pairs of objects in an *M*-by-*N* data matrix *X*, where rows of *X* correspond to the values of variables extracted from a single amygdala image and columns correspond to different variables, was then calculated using the “pdist” function in Matlab. The “linkage” function was then used to create a hierarchical cluster tree using the furthest distance between the clusters from the standardized Euclidean distance matrix calculated using “pdist”. *k*-means clustering was performed using the “kmeans” function in Matlab, which partitions the points in the data matrix *X* into *N* clusters (for example, *N* = 3 for 3 glomeruli) by minimizing the sum, over all clusters, of the within-cluster sums of point-to-cluster centroid distances (squared Euclidean distance). The accuracy of this clustering is assessed by counting how many samples are correctly grouped together by glomerulus type. Calculation of the density of fibres was performed by generating a *Z* projection of the warped and processed images, and using the contour surface function of Imaris (Bitplane) to calculate the pixel density within the lateral and medial halves of the posterolateral cortical amygdala. The boundary between the lateral and medial halves of the posterolateral nucleus was defined by the line extending straight horizontally through the semi-major axis of the posteromedial nucleus (which appears as an ellipse in the warped template brain; see Fig. 4d).

Normalized cross-correlation. Images of piriform cortex and posterolateral cortical amygdala projection patterns were blurred using a Gaussian filter (piriform cortex $\sigma = 200 \mu\text{m}$; amygdala $\sigma = \sim 70 \mu\text{m}$), cropped to exclude areas outside the region of interest, resized (piriform = 500×250 pixels; amygdala = 200×224 pixels), thresholded in Photoshop (Adobe) to binarize pixel values, and converted to grayscale in Matlab. The “normxcorr2” function in Matlab was then used to compute the normalized cross-correlation between the pixel values of two images (for example, MOR1-3 piriform 1 \times MOR1-3 piriform 2) (Supplementary Fig. 8a). This function returns a matrix of Pearson correlation coefficients calculated using the following equation:

$$\gamma(u,v) = \frac{\sum x,y [f(x,y) - \bar{f}, v] [t(x-u, y-v) - \bar{t}]}{\left\{ \sum x,y [f(x,y) - \bar{f}, u]^2 \sum x,y [t(x-u, y-v) - \bar{t}]^2 \right\}^{0.5}}$$

where *f* is the image, \bar{t} is the mean of the template, and \bar{f}, v is the mean of *f*(*x*, *y*) in the region under the template.

By default, non-overlapping pixels in this analysis are assigned a padding value of zero; note that because the means of the template and the source image are subtracted from the pixel values, non-overlapping pixels can still potentially contribute to the correlation coefficient. This matrix of correlation coefficients is then plotted using the “surf” function in Matlab to generate correlograms (Supplementary Fig. 8c), where warmer colours represent high correlation values (close to 1) and cooler colours represent anticorrelation values (close to -1). The cross-correlation between pixel values in two images was calculated when the images were directly superimposed, and calculated again as one image was shifted relative to the other until no more overlap is possible in all directions (Supplementary Fig. 8b). The result of these calculations is a matrix of correlation coefficients that reflects the degree of correlation between the pixel values in two images across the entire range of shifts (until the images are completely non-overlapping), and this matrix can be plotted as a correlogram (Supplementary Fig. 8c). If there is similarity in the spatial patterning in two images, there will be a peak (red colour) in the correlogram that reflects correlation coefficients greater than zero. The

location of this peak in the correlogram is a direct reflection of the similarity between the spatial patterning in two images. Images with similar spatial patterning will have the highest correlation in pixel values when they are directly superimposed, and the result of this is a peak at the centre of the correlogram—the images do not need to be significantly shifted relative to each other for the spatial patterning to overlap. Images with dissimilar spatial patterning will have the highest degree of correlation in pixel values when one is shifted relative to the other (that is, shifting one image relative to the other gets the patterning in the images to overlap), resulting in a peak in the correlogram that is displaced from the centre. The amount the correlogram peak is spatially offset from the centre of the correlogram can be quantified, and used as a measure of the similarity of the spatial patterning in two images (Supplementary Figs 10, 11). Finally, the shape of the peak in the correlogram is related to the nature of the patterning; focal patterning will generate a more focal (circular) peak, whereas more distributed patterning will generate a more elongated peak (that is, there is overlap in the two patterns over a larger range of spatial shifts). For both piriform and amygdala, normalized cross-correlation was performed for all pairwise combinations, in both possible configurations (for example, MOR1-3 \times MOR28 A, and MOR28 A \times MOR1-3 A). The location of the maximum correlation coefficient in correlograms was determined by transforming the matrix of correlation values into a linear array and using the “max” function to find the maximum value in the array, followed by the data cursor feature to find the *X* and *Y* coordinates of the maximum correlation coefficient in each correlogram. For each pairwise comparison, the location of the maximum correlation coefficient for the configuration where the distance between the location of the maximum correlation coefficient and the centre of the correlogram was the smallest was used to generate scatterplots.

Because non-overlapping pixels can potentially be assigned a real number value (due to subtracting of the means) in the calculation of the Pearson correlation coefficient, artefacts can be introduced in the correlogram at the edges, which represent correlation coefficients calculated under conditions where few pixels are overlapping between the template and the source images. We therefore also performed normalized cross-correlation analysis using an alternative data padding method to control for the possibility that the edge artefacts cause changes in the spatial position of the correlogram coefficient maximum. Template images tiled as a 3×3 array (Supplementary Fig. 8d) were generated for all individual images, and the normalized cross-correlation was then calculated for all pairwise combinations of single and tiled images, as previously described. Running the normXcorr2 algorithm using the tiled templates returns a correlogram that resembles a 3×3 grid with additional data points at the edges, but in which the block in the centre has been subject to analysis without the source image ever sliding off into a region that has no overlap. Because the template image is tiled, the region of overlap between the sliding image and the template will always contain the same set of pixel values, though the spatial order of these pixels will be offset. The result is that, for computing the centre block of the 3×3 cross-correlogram, the mean image pixel value and the standard deviation of image pixel values used to calculate the Pearson coefficient are constant as this region of the tiled image slides across the template; this effectively avoids the introduction of the edge artefacts described earlier. The resulting matrices of correlation coefficients were plotted using the “surf” function. These matrices were either left uncropped (and therefore include the correlations between all nine panels plus the edges), were cropped to the equivalent spatial displacements as were generated in the initial analysis with zero padding (and which therefore contain offset peaks that are directly comparable between the two methods), or were cropped such that the source image only was allowed to slide for 50% of its length on any axis across the template image. This final crop limits all of the values in the correlation matrix to those in which half or more of the values in the correlation matrix arise from correlations between the image and the centre tile (rather than the adjacent tiles in the template). The *X*, *Y* coordinates of the maximum correlation coefficient were extracted from the “equivalent” correlograms using the “max” and “find” functions on a submatrix representing the correlation coefficient values within and surrounding the centre peak of the correlogram (for example, the peak closest to the centre of the correlogram, not the peaks near the edge of the correlogram in the equivalent view). Once again, for each pairwise comparison, the location of the maximum correlation coefficient for the configuration where the distance between the location of the maximum correlation coefficient and the centre of the correlogram was the smallest was used to generate scatterplots. The scatterplots generated using the two different methods are qualitatively and quantitatively similar (Supplementary Figs 10, 11 and Supplementary Tables 2, 3), and the correlograms generated by the two methods are qualitatively similar as well (Supplementary Fig. 12), suggesting that our analyses are robust to possible correlation artefacts caused by differences in the degree of pixel overlap between the two methods.

Genetics. Construction of MOR1-3-IRES-GFP animals was achieved as follows: a 7.8-kb genomic clone containing the complete MOR1-3 open reading frame

plus 5.3 kb upstream and 1.5 kb downstream sequence was mutagenized by PCR to insert a *PacI* restriction site 5 bp after the stop codon. An IRES-GFP-ACN cassette was cloned into the *PacI* site to prepare the targeting vector³³. After electroporation into 129SvEv-derived mouse embryonic stem cells, genomic DNA from G418-resistant colonies was screened by Southern blotting with *AflII* to detect homologous recombination using a 400 bp probe 5' of the targeting vector (7.4 kb wild-type allele versus 12.7 kb targeted allele). Chimaeras obtained from recombinant clones by standard mouse procedures were mated to C57BL/6J females to obtain heterozygous MOR1-3-IRES-GFP mice that had deleted the *neo^R* selection marker in the male germline. Construction of the MOR174-9-IRES-GFP animals was achieved as follows: two genomic fragments containing the MOR174-9 5' flanking sequence plus open reading frame (3.4 kb, *XmaI* sites) and 3' flanking sequence (2.7 kb, *SalI* sites) were isolated by PCR from mouse genomic DNA, with restriction sites present in the primers. These two homologous arms were cloned into an IRES-GFP-ACN vector to obtain the targeting construct. Homologous recombinant clones were identified by *EcoRI*-digested genomic DNA blots (5.2 kb wild-type allele versus ~10 kb targeted allele) using a 300 bp probe 5' of the construct. Mice were obtained from recombinant embryonic stem cells as described for MOR1-3-IRES-GFP strain. MOR28-IRES-GFP was previously described³⁴. Note that MOR28 is also known as both MOR244-1 and Olfr1507; MOR1-3 is also known as Olfr66; and MOR174-9 is also known as

Olfr73. The OMP-IRES-spH and M72-IRES-GFP animals were obtained from the Jackson Labs.

26. Haberly, L. B. & Price, J. L. The axonal projection patterns of the mitral and tufted cells of the olfactory bulb in the rat. *Brain Res.* **129**, 152–157 (1977).
27. Scott, J. W., McBride, R. L. & Schneider, S. P. The organization of projections from the olfactory bulb to the piriform cortex and olfactory tubercle in the rat. *J. Comp. Neurol.* **194**, 519–534 (1980).
28. Scott, J. W. Electrophysiological identification of mitral and tufted cells and distributions of their axons in olfactory system of the rat. *J. Neurophysiol.* **46**, 918–931 (1981).
29. Schneider, S. P. & Scott, J. W. Orthodromic response properties of rat olfactory bulb mitral and tufted cells correlate with their projection patterns. *J. Neurophysiol.* **50**, 358–378 (1983).
30. Skeen, L. C. & Hall, W. C. Efferent projections of the main and the accessory olfactory bulb in the tree shrew (*Tupaia glis*). *J. Comp. Neurol.* **172**, 1–35 (1977).
31. Emmenlauer, M. *et al.* XuvTools: free, fast and reliable stitching of large 3D datasets. *J. Microsc.* **233**, 42–60 (2009).
32. Datta, S. R. *et al.* The *Drosophila* pheromone cVA activates a sexually dimorphic neural circuit. *Nature* **452**, 473–477 (2008).
33. Bunting, M., Bernstein, K. E., Greer, J. M., Capocchi, M. R. & Thomas, K. R. Targeting genes for self-excision in the germ line. *Genes Dev.* **13**, 1524–1528 (1999).
34. Shykind, B. M. *et al.* Gene switching and the stability of odorant receptor gene choice. *Cell* **117**, 801–815 (2004).